

Additive Manufacturing of Single-Crystal Superalloy CMSX-4 Through Scanning Laser Epitaxy: Computational Modeling, Experimental Process Development, and Process Parameter Optimization



AMRITA BASAK, RANADIP ACHARYA, and SUMAN DAS

This paper focuses on additive manufacturing (AM) of single-crystal (SX) nickel-based superalloy CMSX-4 through scanning laser epitaxy (SLE). SLE, a powder bed fusion-based AM process was explored for the purpose of producing crack-free, dense deposits of CMSX-4 on top of similar chemistry investment-cast substrates. Optical microscopy and scanning electron microscopy (SEM) investigations revealed the presence of dendritic microstructures that consisted of fine γ' precipitates within the γ matrix in the deposit region. Computational fluid dynamics (CFD)-based process modeling, statistical design of experiments (DoE), and microstructural characterization techniques were combined to produce metallurgically bonded single-crystal deposits of more than 500 μm height in a single pass along the entire length of the substrate. A customized quantitative metallography based image analysis technique was employed for automatic extraction of various deposit quality metrics from the digital cross-sectional micrographs. The processing parameters were varied, and optimal processing windows were identified to obtain good quality deposits. The results reported here represent one of the few successes obtained in producing single-crystal epitaxial deposits through a powder bed fusion-based metal AM process and thus demonstrate the potential of SLE to repair and manufacture single-crystal hot section components of gas turbine systems from nickel-based superalloy powders.

DOI: 10.1007/s11661-016-3571-y

© The Minerals, Metals & Materials Society and ASM International 2016

I. INTRODUCTION

NICKEL-BASED superalloys are used extensively in gas turbine engines for the manufacture of hot section components primarily because of their superior properties such as excellent mechanical strength, higher resistance to thermal creep deformation, corrosion, oxidation, and good surface stability in elevated temperature environments. Typical nickel-based superalloys used in gas turbine engines contain several alloying elements to optimize the material for the best possible performance in aggressive loading scenarios. These superalloys have higher yield strength due to the presence of secondary γ' phases that precipitate within

the γ phase and form an anti-phase boundary prohibiting the dislocation or partial dislocation movements.^[1] Turbine components cast with a polycrystalline or equiaxed (EQ) morphology are susceptible to failure because they contain grain boundaries that are transverse to the direction of applied load. Voids are likely to form at these transverse grain boundaries.^[1] To alleviate this problem, directionally solidified (DS) morphologies are used where the resulting grain structure is parallel to the major axis of loading and contains a limited number of transverse grain boundaries. Elimination of these transverse grain boundaries results in additional creep and rupture strength. In addition, alignment of the grain structures provides a favorable modulus of elasticity in the loading direction, thereby enhancing the fatigue life. Creep strength and fracture toughness can be further enhanced by casting the blade with a single-crystal (SX) morphology that contains no grain boundaries at all. The single-crystal morphology also allows removal of grain boundary strengthening elements such as carbon and boron that are typically responsible for reducing the melting temperature and the fatigue life of the alloy.^[2]

CMSX-4 is a rhenium containing second-generation ultrahigh-strength SX superalloy developed through the joint efforts of Canon-Muskegon and Allison. The alloy demonstrates a 308.15 K (35 °C) turbine airfoil temperature capability improvement compared to the first

AMRITA BASAK, Graduate Student, is with George W. Woodruff School of Mechanical Engineering, Georgia Institute of Technology, 801 Ferst Drive, Atlanta, GA, 30332-0405. RANADIP ACHARYA, formerly Ph.D. Student with the George W. Woodruff School of Mechanical Engineering, Georgia Institute of Technology, is now Senior Research Engineer with United Technologies Research Center, 411 Silver Ln, East Hartford, CT 06118. SUMAN DAS, Morris M. Bryan, Jr. Chair in Mechanical Engineering for Advanced Manufacturing Systems; Director, Direct Digital Manufacturing Laboratory, is with George W. Woodruff School of Mechanical Engineering, Georgia Institute of Technology, and also with the School of Materials Science and Engineering, Georgia Institute of Technology, 771 Ferst Drive NW, Atlanta, GA 30313. Contact e-mail: sumandas@gatech.edu

Manuscript submitted January 13, 2016.

Article published online June 14, 2016

generation single-crystal alloys such as CMSX-2 and CMSX-3.^[3] The addition of rhenium delays coarsening of the γ' phase, and increases γ/γ' misfit.^[4] Clustering of rhenium was initially believed to act as an obstacle against dislocation movements, resulting in an improvement in the superalloy strength.^[5] However, recent studies using atom probe tomography have failed to find evidence of rhenium clusters in the γ phase, γ/γ' interfaces, and in the center of the γ channels of the CMSX-4 superalloy.^[6] CMSX-4 is strengthened by the solid solution-strengthening effects of chromium (Cr), tungsten (W), and tantalum (Ta). The presence of aluminum (Al) and titanium (Ti) provides additional strength due to the precipitation-hardening effects of the γ' phase.^[7] Although this second phase is the main reason for the improvement in properties, it also results in increased processing difficulties. These alloys are prone to crack formation and, therefore, hard to cast. Strain age cracking is also observed during welding and is a consequence of the precipitation of γ' phases, hardening of the alloy during thermal exposure, and transfer of solidification strains onto the grain boundaries. The susceptibility to strain age cracking and the alloy weldability are often qualitatively described for nickel-based superalloys by plotting Al vs Ti content in the alloys.^[8] The alloy is considered “non-weldable” if the total Al+Ti content exceeds 4 wt pct. The total Al+Ti content in CMSX-4 is 6.6 wt pct, thus making it a “non-weldable” alloy.

A single-crystal deposit formed through an additive process can be characterized by several microstructural parameters such as the primary dendrite arm spacing (PDAS), the columnar-to-equiaxed transition (CET), the oriented-to-misoriented transition (OMT), and the presence of stray grains (SG). An increase in the dendrite arm spacing adversely affects the high-cycle fatigue life. Fatigue cracks are found to originate at shrinkage porosity and the largest pores are correlated with a large PDAS.^[9] During solidification, the solidified region acts as a heat sink, and the temperature gradient ahead of the solidification front decreases, resulting in a change from the single-crystal microstructure to an equiaxed microstructure. This change is referred to as the columnar-to-equiaxed transition (CET). CET limits the epitaxial single-crystal growth and makes the deposit near the top surface polycrystalline in nature.^[10] A second solidification phenomenon, known as the oriented-to-misoriented transition (OMT), occurs when there is a change in the direction of the temperature gradient in the solidifying metal. This occurs primarily because of the competition between the possible columnar growth directions.^[11] Both CET and OMT are critical to the quality of the single-crystal deposit as they limit the single-crystal (SX) height. Existing literature reveals that the local inhomogeneity in the temperature gradient and the solidification velocity or the presence of broken dendritic arms and subsequent convection of those broken pieces acts as sources of new nucleation sites that result in the formation of stray grains (SG). Due to segregation of γ/γ' eutectics, a liquid film forms around the SG boundary. Such formation results in higher grain boundary wetting making the material prone to cracking.^[12]

Repair attempts on superalloys started in the late sixties using different welding processes. The most commonly used processes are gas tungsten arc (GTA) welding or tungsten inert gas (TIG) welding, electron beam (EB) welding, and laser welding. However, the introduction of single-crystal superalloys necessitated the development of new repair techniques as the usage of existing welding processes such as TIG resulted in the formation of stray grains (SG)^[13] as well as cracking.^[14] Limited literature is available on the repair of single-crystal hot section components using AM based processes primarily due to the tremendous processing challenges associated with these alloy systems. Achieving single-crystal microstructure is challenging and requires tight control of the processing parameters such as energy source power, scan speed, and spot diameter. Sufficient remelting of the underlying substrate is required along with columnar dendrite growth in the newly consolidated material to form SX deposits.

Epitaxial laser metal forming (ELMF) was the first AM process to demonstrate the formation of multiple single-crystal layers of CMSX-4 on top of like chemistry substrates.^[15] Similar results were also obtained for dissimilar material systems such as M-Cr-Al-Y^[16] and Ni-Cr-Al-Y^[17] depositions on CMSX-4 and SRR99 substrates, respectively. SX deposits of René N4 on CMSX-4 substrates were produced using the direct metal deposition (DMD) process where the deposits grew epitaxially from the substrate.^[18] Powder bed-based electron beam melting (EBM) process was applied to process René 142 powders where epitaxial DS microstructure of more than 400 μm was obtained.^[19] The CMSX-4 powder was processed through EBM process and the resultant microstructure followed SX morphology.^[20] The powder blowing mechanism used for cladding or directed metal deposition processes are typically limited by the speed of the mechanical powder feed assembly that limits the speed at which the energy source can scan across the substrate. In addition to this, in laser cladding processes, the high-velocity powder particles can disturb the convective flow inside the melt pool and act as new nucleation sites that disrupt the single-crystal structure while promoting the formation of stray grains (SG).

Simulations can provide valuable insights into understanding the physics of the AM process. Approaches based on finite volume methods (FVM)^[21] and finite element methods (FEM)^[22] have extensively been employed for thermal modeling of the system. A CFD-based model allows simulation of convection inside the melt pool.^[23] The shape of the deposited layers has been predicted using modified immersed boundary method with a finite difference scheme.^[24] Level set methods have also been attempted recently to track the free surface motion of the molten pool with the powder material feeding and scanning of the laser beam for multi-layer cladding.^[25] A coupled flow-thermal model was developed in order to simulate the conditions inside laser melt pool while considering surface tension gradient-driven flows known as Marangoni convection (or Bernard-Marangoni convection).^[26] These models represent a single weld bead and do not consider the effect of high-speed raster scanning on the melt pool.

The raster scan employed in SLE changes the shape of the melt pool from an ellipsoid^[27] to a convex hull.^[28] Acharya *et al.* developed a three-dimensional (3D) CFD model incorporating the raster scanning strategy and obtained good agreement with experimental data for the melt depth in CMSX-4 processed through SLE.^[28] Acharya *et al.* implemented a two-dimensional (2D) approach to simulate the melt pool characteristics for IN100 and obtained good agreement for the melt depth, the average melt pool temperature, and the melt pool area.^[29]

Scanning laser epitaxy (SLE), a direct descendant of the selective laser sintering (SLS) for metals developed in the late 1990s,^[30] is a powder bed fusion-based additive manufacturing process that uses a high-power tightly controlled fiber laser beam to initiate a melt pool by performing raster scans that are adaptable to the geometry under consideration. The melt pool travels along the length of the substrate fusing the partially melted substrate to the fully melted pre-placed powder that lies on top of the substrate. SLE has been demonstrated to maintain epitaxy between the substrate and the newly formed deposit, and thus, the process has shown significant potential allowing one step repair of single-crystal nickel-based superalloy CMSX-4.^[28,31] This study was performed using a continuous wave 1064 nm 2.4 kW Nd:YAG laser that produced a 1.5-mm-diameter Gaussian spot size. Fiber lasers can provide a much smaller beam diameter at high mean powers compared to Nd:YAG lasers. A large beam diameter (*D*) is not economical since the reduced beam intensity rapidly limits the process. Thus, when a large *D* is inevitable, it is necessary to increase the laser power in order to achieve sufficient remelting of the substrate to ensure a continuous metallurgical bond. The requirement for tighter beam diameter control to aid real-life complex turbine blade processing has necessitated the use of a fiber laser that has shown encouraging results with regard to the processing of the “non-weldable” equiaxed superalloys IN100^[29] and René 80.^[32]

In the present study, the single-pass deposition of SX CMSX-4 superalloy using a high-power fiber laser beam of 20 μm Gaussian beam radius utilizing a powder bed of thickness exceeding 1000 μm was demonstrated. The microstructural investigation revealed the capability of SLE to produce dense, crack-free deposits for CMSX-4 that resulted in more than 500 μm of SX deposits in a single pass. The structure of the deposits was investigated through optical microscopy and scanning electron microscopy (SEM). Acharya’s model^[29] was extended to simulate melt pool characteristics for CMSX-4. The CFD model was validated using quantitative metallography and thermal data obtained from an IR camera. Excellent agreement between the simulation and the experimental results was achieved for the melt depth, the average melt pool temperature, and the melt pool area. The melt back depth was a critical parameter in the present study as it controlled the quality of the metallurgical bond between the substrate and the deposit. In addition, for SX components, sufficient amount of melt back was required to ensure SX growth from the partially melted substrate. Multiple CFD simulations

were performed to select the SLE processing parameter ranges to achieve the desired melt back depth before performing costly design of experiment (DoE)-based experimental runs. The DoE trials were performed to study the effects of various SLE processing parameters on the deposit quality and an operating regime was identified to obtain desired SX deposits. A previously developed MATLAB code was applied to extract necessary information from the digital images using quantitative metallography techniques.^[33]

II. EXPERIMENTAL PROCEDURE

In the experimental setup, a single-mode 1kW Ytterbium fiber laser (IPG Photonics, model: YLS-1000) was used with a 3-axis galvanometer scanning system (Cambridge Technology) to process the substrate coupons inside a controlled-atmosphere processing chamber. A thermal imaging camera and a melt pool video microscope were used to measure the melt pool temperature and to capture a video of the SLE processing, respectively. The fiber laser was focused through the 3-axis galvanometer scanner to a spot size of 20 μm Gaussian beam radius, enabling tight control of the energy density. The typical scan speeds used in SLE were of the order of hundreds of mm/s although the scanner had the ability to move the laser beam at speeds of up to several m/s. The raster scan pattern with alternate scan vector is illustrated in Figure 1(b) for the coupon placed in position 2. After each pass, the laser moved over by the scan spacing and started traveling along the direction opposite to the previous scan path.

The SLE process was conducted inside a controlled-atmosphere process chamber purged to less than 10 parts-per-million (PPM) oxygen at atmospheric pressure using 99.999 pct high-purity Argon. The substrate coupons and the pre-placed powder were initially at ambient temperature, and no pre-heating was done prior to the SLE processing. The process was carried out on rectangular investment-cast SX CMSX-4 coupons having dimensions of 35.56 mm \times 6.86 mm \times 2.54 mm with $\langle 001 \rangle$ columnar orientations. Each substrate was placed inside a 35.56 mm \times 6.86 mm recession cut into an IN625 base plate. The thickness of the powder bed was kept fixed at 1.4 mm. Figure 1(a) shows an overview of the SLE process equipment, and Figure 1(b) shows the placement of substrate coupons and powder bed on top of it. Hereafter, the substrate coupon with the pre-placed powder fused to it after SLE processing is referred to as ‘sample.’

A. Materials

The CMSX-4 powder used in this study was produced by the Praxair Surface Technologies. It was an argon gas-atomized powder, and the composition is reported in Table I. The morphology, size distribution, and cross-sections of powders were analyzed using optical microscopy and SEM. The CMSX-4 powder particles were mostly spherical with particle diameter varying from 90 to 150 μm as shown in Figure 2(a). The powder

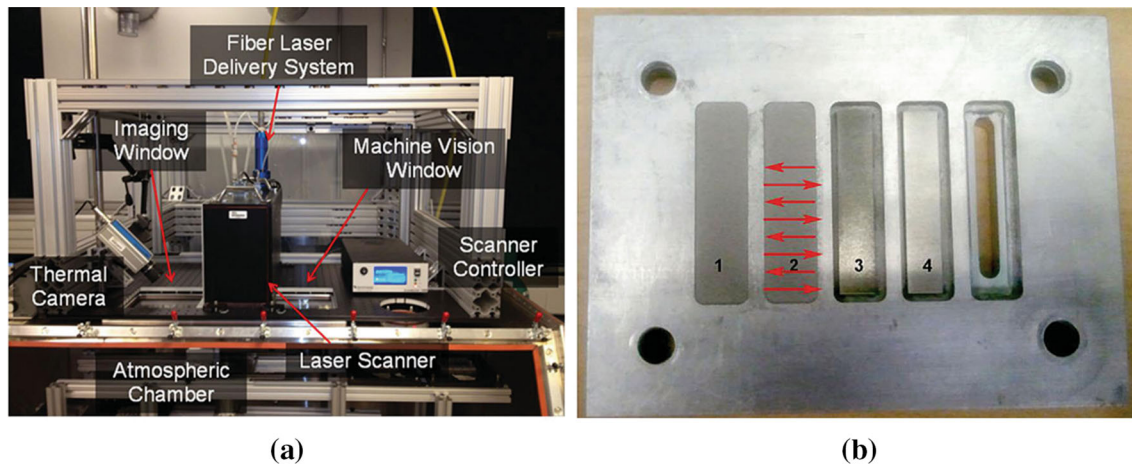


Fig. 1—(a) The SLE workstation (b) placement of superalloy coupons in the SLE process. The rightmost position shows the blank base to simulate the hollow passages below the tip in high-pressure turbine blades. Positions 3 and 4 show bare substrate coupons, and positions 1 and 2 show substrate coupons with pre-placed powder on top. The rastering movement of the scan is shown for the coupon in position 2 (Color figure online).

Table I. Composition of the CMSX-4 Powder (Weight Percent)

	Cr	Co	Mo	Re	W	Al	Ti	Ta	Hf	B	C	Zr	Ni
CMSX-4	6.5	9.7	0.4	3.0	6.4	5.6	1.0	6.5	—	—	—	—	Bal

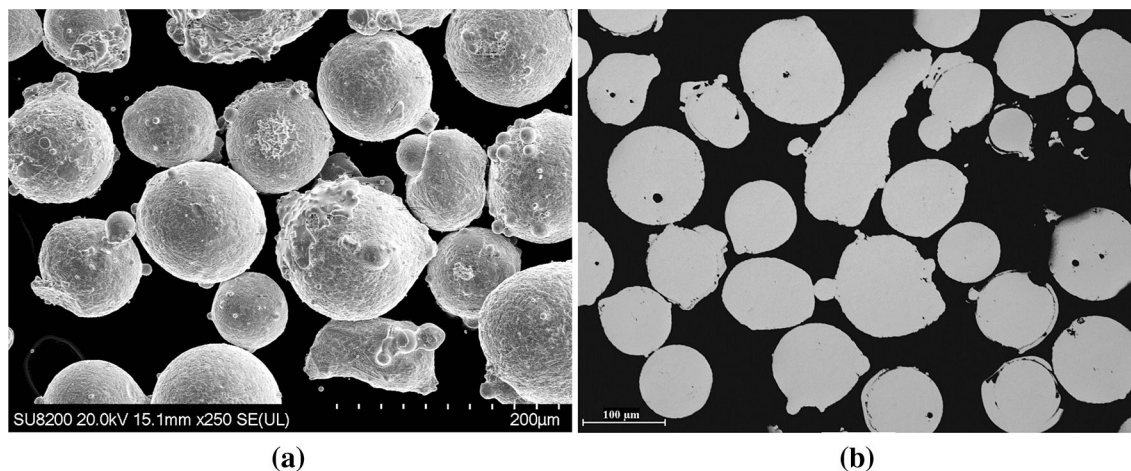


Fig. 2—(a) SEM image of the CMSX-4 powder and (b) optical microscopic image of the CMSX-4 powder cross-section after polishing.

was mounted in Bakelite and polished to a mirror finish. The cross-section was analyzed under an optical microscope for the inspection of internal porosity. Limited internal porosity was detected as shown in Figure 2(b).

B. Methods

1. Optical microscopy

A Buehler automated saw was used to section the samples for microstructural investigation. Each section was mounted in Bakelite and polished to a mirror finish, starting with 80 grit paper and progressively increasing the size to 1200 grit. The samples were then polished using 5- and 3- μm diamond solutions. Finally, the

samples were polished using a 0.5 μm colloidal alumina suspension. The polished samples were then etched with Marble's reagent (50 ml HCl, 50 ml H₂O and 10.0 gm CuSO₄) to remove the γ' phase revealing the dendritic microstructure. Imaging was then completed using a Leica DM6000 optical microscope at 100 \times magnification.

2. Quantitative image analysis

Each sample was analyzed to determine the SX ratio, the average deposit height, the deposit height uniformity, the number of stray grains, the melt back depth, and the lack of deformation of the substrate. In this study, the SX ratio was defined as the ratio of the

average SX height to the average of the total deposit height. A customized image analysis code written in MATLAB (The MathWorks Inc., Natick, MA, USA) was used to extract all the metrics that were essential for the DoE-based process parameter optimization.^[33]

3. Scanning electron microscopy (SEM)

SEM investigation was carried out on a Hitachi SU8230 SEM to characterize the microstructural composition of the SLE-processed CMSX-4 deposit. Marble's reagent (50 ml HCl, 50 ml H₂O and 10.0 gm CuSO₄) was again used. The Marble's reagent preferentially attacked the γ' precipitate phase and left the residual γ channels visible for metallographic investigations.

III. COMPUTATIONAL MODELING

A two-dimensional (2D) transient, multi-domain model with temperature-dependent thermo-physical properties is used to simulate the flow-thermal behavior of the SLE process to predict the melt pool characteristics. The CFD model has been previously applied to simulate the flow-thermal behavior of equiaxed superalloy IN100.^[29]

A. Geometry and Mesh

The pseudo-2D model included two separate domains—(1) the deposit domain consisting of the substrate at the bottom and the powder layer at the top and (2) the IN625 baseplate domain as shown in

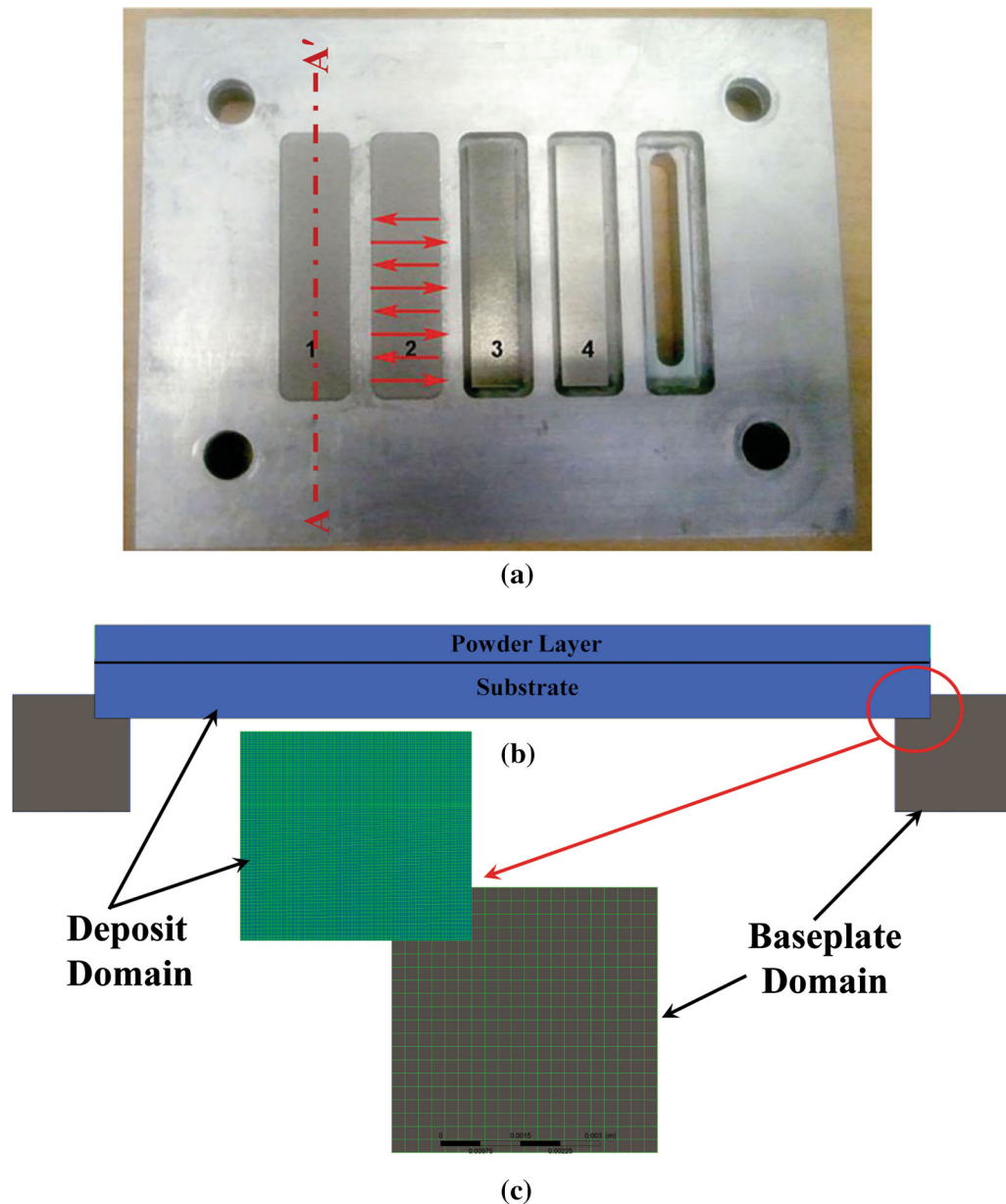


Fig. 3—(a) Experimental coupon setup showing the section plane location AA' that generates the pseudo-CFD domain; ANSYS CFX simulation model showing (b) deposit domain and baseplate domain, and (c) mesh details in the deposit and the baseplate domain (Color figure online).

Figure 3(b). The domain was obtained by taking a section at AA' as shown in Figure 3(a). The sectioning direction is perpendicular to the plane of the paper.^[34] Figure 3(b) shows the geometry and mesh for the 2D configuration. The deposit domain had a finer mesh to accurately capture the 20 μm radius laser heat source. The total node count of the mesh was close to 137k, and the skewness was below 0.2. The simulation was performed in ANSYS CFX solver.

B. Flow Physics and Boundary Conditions

The solid and liquid component enthalpy equations, expressed in terms of volume fractions, r , are

$$\frac{\partial(\rho_S r_S h_S)}{\partial t} + \nabla \cdot (\rho_S r_S \underline{U}_S h_S) = \nabla \cdot (r_S k_S \nabla T_S) + I, \quad [1a]$$

$$\frac{\partial(\rho_L r_L h_L)}{\partial t} + \nabla \cdot (\rho_L r_L \underline{U}_L h_L) = \nabla \cdot (r_L k_L \nabla T_L) - I, \quad [1b]$$

Here ρ is the density, h is the enthalpy (including the latent heat), T is the temperature, \underline{U} is the velocity, and I is the interphase heat transfer. The subscripts S and L refer to the solid and liquid components respectively. Equations [1a] and [1b] can also be expressed more compactly as

$$\begin{aligned} \frac{\partial(\bar{\rho}h)}{\partial t} + \nabla \cdot (\bar{\rho}\underline{U}h) &= \nabla \cdot (\bar{k}\nabla T) \\ &- \nabla \cdot (\bar{\rho}Y_S(\underline{U} - \underline{U}_S)(h_L - h_S)) + S \end{aligned} \quad [2]$$

Here $\bar{\rho}$ is mixture density, h is the mixture enthalpy, \bar{k} is mixture conductivity, and Y_S is the mass fraction of solid.^[35] The final term in Eq. [2] represents an additional source due to the difference in velocity between the solid and the liquid components. This term has a finite value in the mushy region of the flow ($0 < Y_S, Y_L < 1$). In the

regions of pure liquid or pure solid, the mixture enthalpy equation reduces to the appropriate component enthalpy equation.

The volume fractions of liquid and solid components were incorporated using tabular data representing the solid and liquid fraction of the superalloys in the melting range. The Boussinesq approximation was implemented to model the effect of variable liquid density. A Darcy-like source term was incorporated to model the resistance to flow in the mushy region. The permeability was modeled using Kozeny–Carman equation.^[36] To prevent division by zero, the term is bounded by a user-specified maximum, C :

$$\underline{S}_M = \min\left(C, \frac{\mu_L(1-r_L)^2}{K_0 r_L^3}\right) (\underline{U} - \underline{U}_S). \quad [3]$$

In the turbulence equations, sink terms similar to the Darcy term in the momentum equation were applied to damp the turbulence in solid regions^[35]:

$$S_k = -\frac{\mu_L(1-f_L)^2}{K_0 f_L^3} k, \quad S_\epsilon = -\frac{\mu_L(1-f_L)^2}{K_0 f_L^3} \epsilon. \quad [4]$$

Marangoni convection was implemented by imposing a surface tension-driven shear force at the free surface through the following equations^[37]:

$$\mu \frac{\partial U_x}{\partial x} = r_L \frac{\partial \gamma}{\partial T} \frac{\partial T}{\partial x}, \quad \mu \frac{\partial U_y}{\partial y} = r_L \frac{\partial \gamma}{\partial T} \frac{\partial T}{\partial y}. \quad [5]$$

For the baseplate domain, the conduction heat equation was solved:

$$\frac{\partial(\rho H)}{\partial t} = \nabla \cdot (K \nabla T) + S_0. \quad [6]$$

Here ρ is the density, H is the enthalpy, K is the thermal conductivity, and S_0 is the source/sink term.

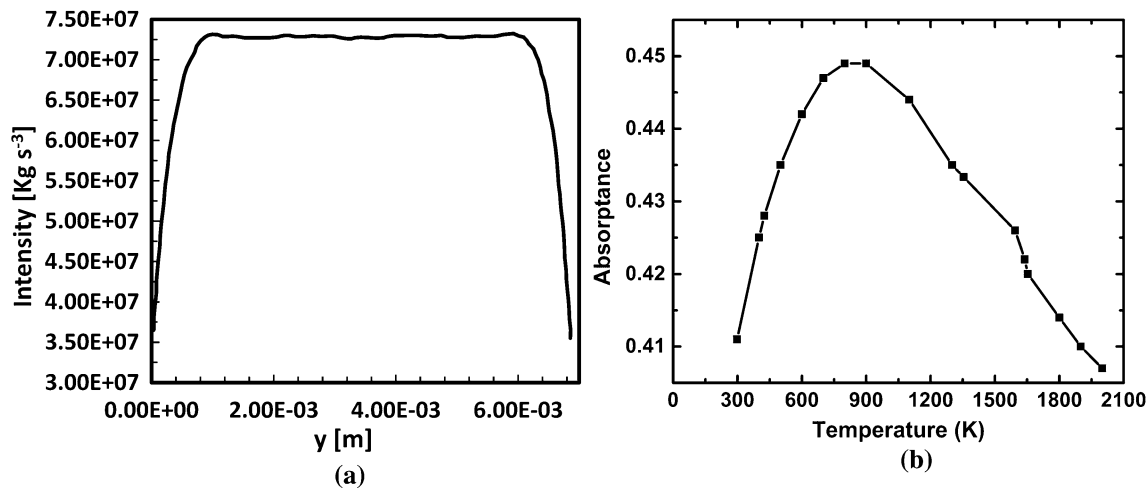


Fig. 4—(a) Representative laser heat source intensity variation in the y -direction obtained from the 3D model^[34] and (b) variation of absorbance as function of temperature for CMSX-4.

The laser heat source was modeled as a Gaussian moving heat source in 3D.^[28] The spatial profile in the y-direction was averaged over a single scan length over the sample width and fitted with a 10th-degree polynomial. This particular profile was then used as a line source with Gaussian distribution applied in the x-direction. The polynomial used for the laser heat source intensity in the y-direction was found to be flat in the middle region with some reduction of intensity near the edges of the sample as shown in Figure 4(a).^[34] This small variation in y-direction was neglected while modeling the problem physics in 2D. This line source represented the term *S* in Eq. [2].

Thermal energy was conserved at all interfaces. A surface sink using Newton's law of cooling was used to model the convection heat loss. Radiation loss was also

modeled using a sink term. The transient model was solved using a time step value approximately equal to 0.002 second. The inclusion of Marangoni convection, phase change models, and Darcy sink terms required a smaller time step value for solver stability. The convergence was assured once the RMS value of residuals was reduced below 1×10^{-4} . Once solved, the result was post-processed in CFD-post to analyze the melt pool nature, the melt depth profile, and the temperature distribution.

C. Material Properties

Thermo-physical property data for liquid and solid phase CMSX-4 were accurately modeled using tabular data.^[38] The properties for IN625 were also modeled

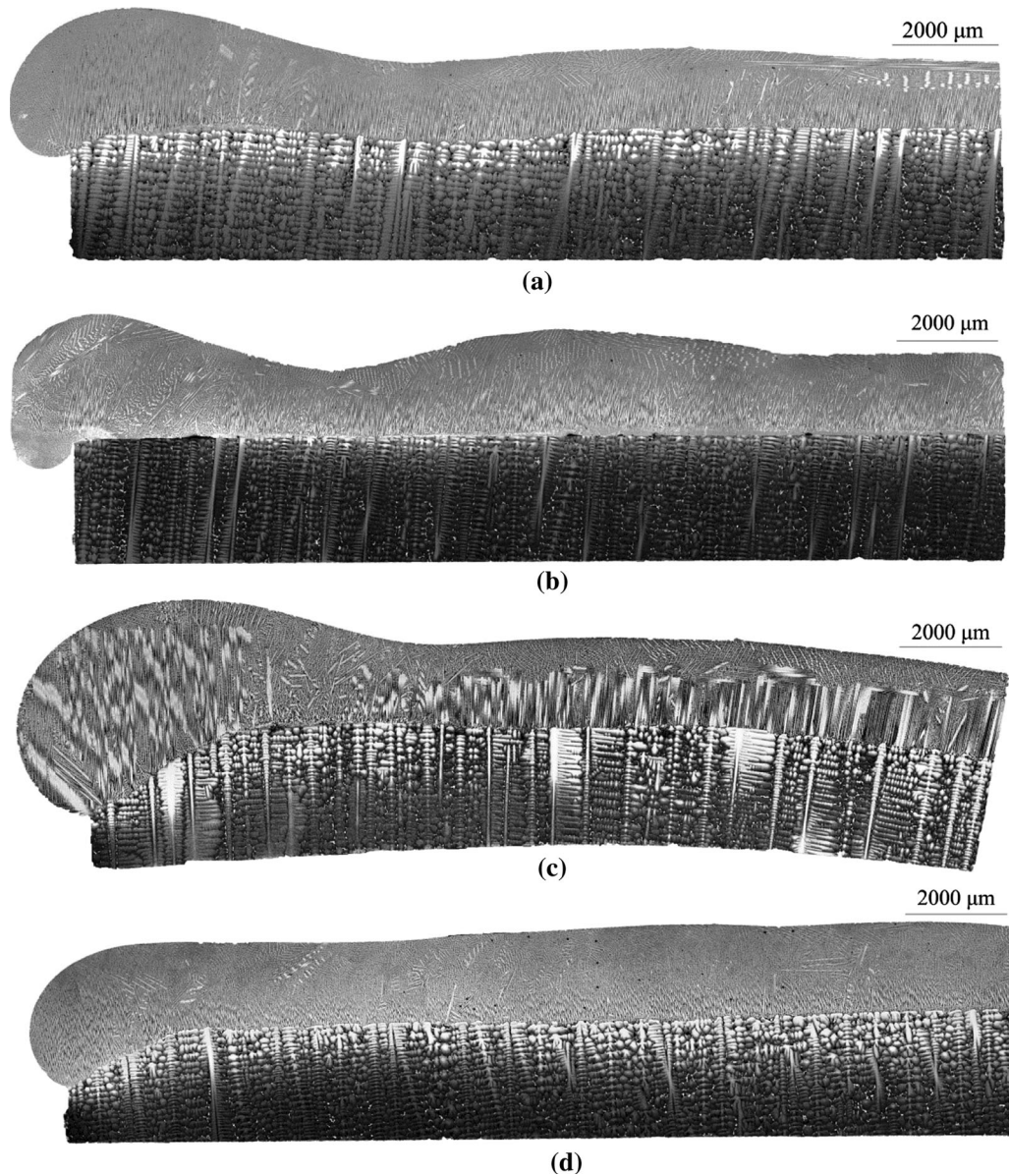


Fig. 5—Representative transverse optical micrographs of CMSX-4 samples showing (a) crack-free and dense deposit, (b) lack of fusion at the starting edge due to reduced number of repeat scans, (c) deformation/warping due to higher scan speed, and (d) lower single-crystal height due to lower scan spacing.

using tabular data.^[8] The absorptance of laser energy was modeled using the Hagen–Rubens relationship.^[39] Since this relationship did not account for the powder phase, a discrepancy was expected during the repeat scan period as the laser beam could directly interact with the powder. However, repeat scans in SLE ensured the formation of a continuous melt pool at the leading edge of the substrate. Hence, the Hagen–Rubens relationship could provide a reasonable estimation of the absorptivity.^[39] Figure 4(b) describes the variation of absorptance for CMSX-4 as a function of temperature. The temperature-dependent values marked by square bullets in Figure 4(b) were used as tabular data in CFX to perform the simulation.

IV. DESIGN OF EXPERIMENT (DOE)-BASED STUDY

In SLE, a melt pool is initiated by the raster scan pattern across the width of the sample. The melt pool propagates linearly along the length of the substrate fusing powder to the substrate. The number of repeat scans, the laser power, the scan speed and the scan

spacing were varied in SLE. The number of repeat scans was defined as the number of raster movements that the laser performed at the leading edge of the sample without moving in the forward direction during the start of the scan process. The laser power and scan speed determined the amount of energy being applied while the number of repeat scans affected the formation of a melt pool at the leading edge of the substrate. Sufficient number of repeat scans was required to pre-heat the underlying substrate and ensure a continuous metallurgical bond across the entire length of the substrate.

The SLE process parameters were combined into two different measures—the total repeat scan energy and the scan energy density. The total repeat scan energy was of immense interest as it determined whether or not a good metallurgical bond was formed between the deposit and the substrate from the beginning of the scan, whereas the scan energy density played a critical role in maintaining the deposit quality along the entire length of the substrate. The total repeat scan energy was calculated as

$$Q = \frac{P \times N}{V_s} \quad [7]$$

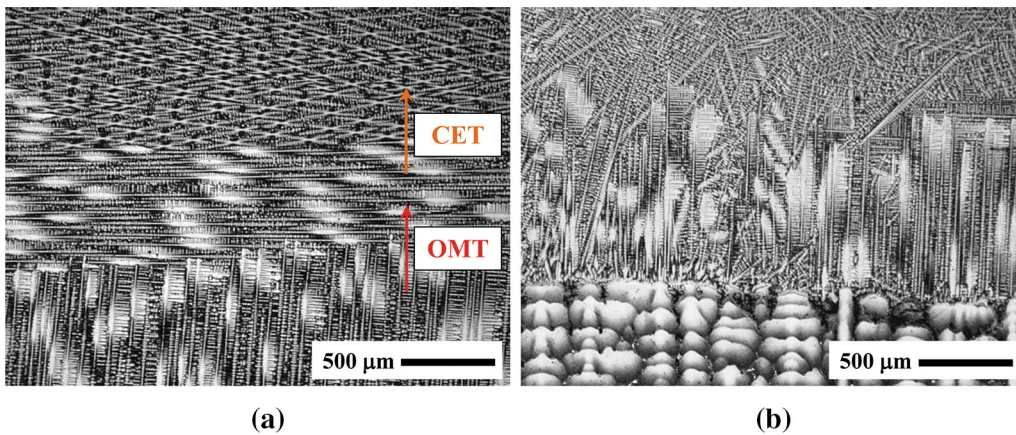


Fig. 6—Representative transverse optical micrograph of CMSX-4 sample showing (a) oriented-to-misoriented transition (OMT) and columnar-to-equiaxed transition (CET), and (b) stray grain (SG) morphology (Color figure online).

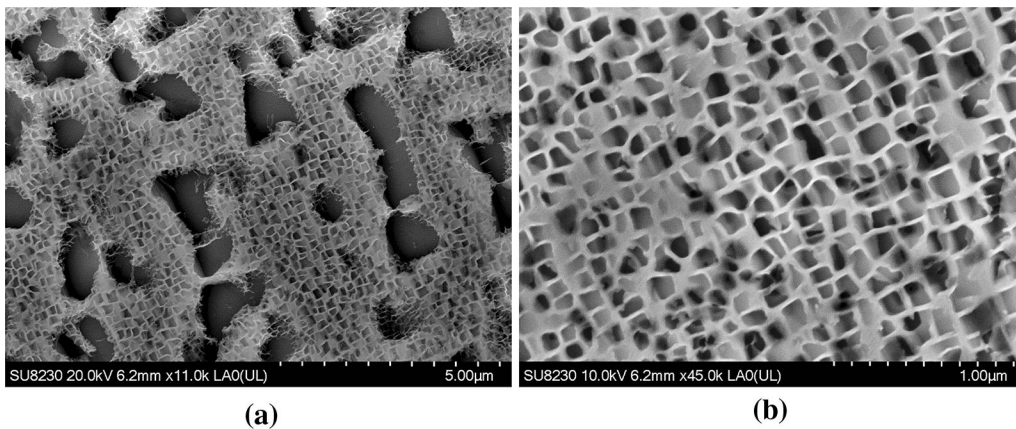


Fig. 7—Representative scanning electron microscopy (SEM) image showing γ/γ' morphology in the (a) substrate region, and (b) deposit region.

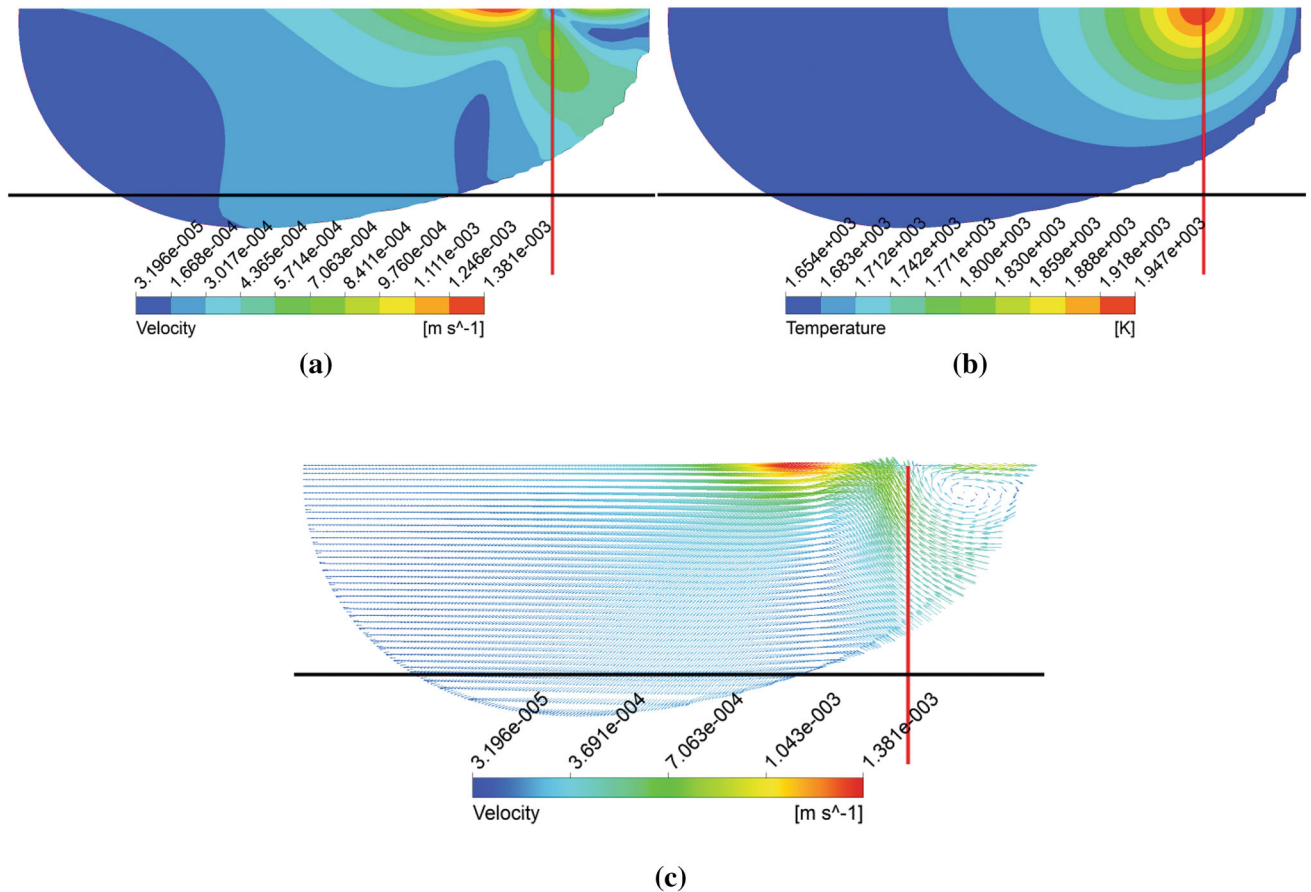


Fig. 8—Representative contours of (a) velocity, (b) temperature, and (c) velocity vectors due to the moving heat source for CMSX-4 inside the melt pool. The black lines indicate the original substrate position before laser processing, and the red lines indicate the instantaneous position of the laser. Laser movement direction is from the left to the right (Color figure online).

Similarly, the scan energy density was defined as

$$E = \frac{P}{SS \times V_s \times t_p} \quad [8]$$

Here P is the laser power, N is the number of repeat scans, V_s is the raster scan speed, SS is the raster scan spacing, and t_p is the powder thickness.

The effects of various processing parameters on metrics such as the SX ratio, the average deposit height, the deposit height uniformity, the number of stray grains, the melt back depth, and the lack of deformation were assessed. The “lack of deformation” was calculated by developing a linear fit for the bottom edge of the substrate and then calculating the average R^2 or goodness of fit between the initial horizontal line and the linear fit. The higher the R^2 value, the less deformed was the substrate, and hence, this parameter was termed “lack of deformation.” The deposit uniformity was also calculated following the aforementioned procedure. The details of the calculation procedure are given elsewhere and skipped here for brevity.^[29]

V. RESULTS AND DISCUSSION

A. Analysis of the SLE Deposition Through Optical Microscopy

The SLE-deposited CMSX-4 samples were analyzed using optical microscopy to investigate the overall deposition characteristics. Figure 5(a) shows the transverse microstructure of a typical SLE-processed CMSX-4 sample demonstrating an excellent metallurgical bond between the substrate and the deposit region. The SLE-processed CMSX-4 deposit was demonstrated to be crack free and dense as shown in Figures 5(a) through (d). Lack of a sufficient number of repeat scans resulted in discontinuous substrate-powder metallurgical bond (Figure 5(b)); however, too many repeat scans caused excessive melt back near the starting edge as shown in Figure 5(c). Similarly, if the scan speed was too high, there would be a thermal lag in the substrate region, resulting in deformation or warping of the sample as shown in Figure 5(c). Inhomogeneity in the local flow field due to excessive raster scan speed or lower power could promote stray grain formation thwarting epitaxial SX growth (Figure 5(c)). Lower

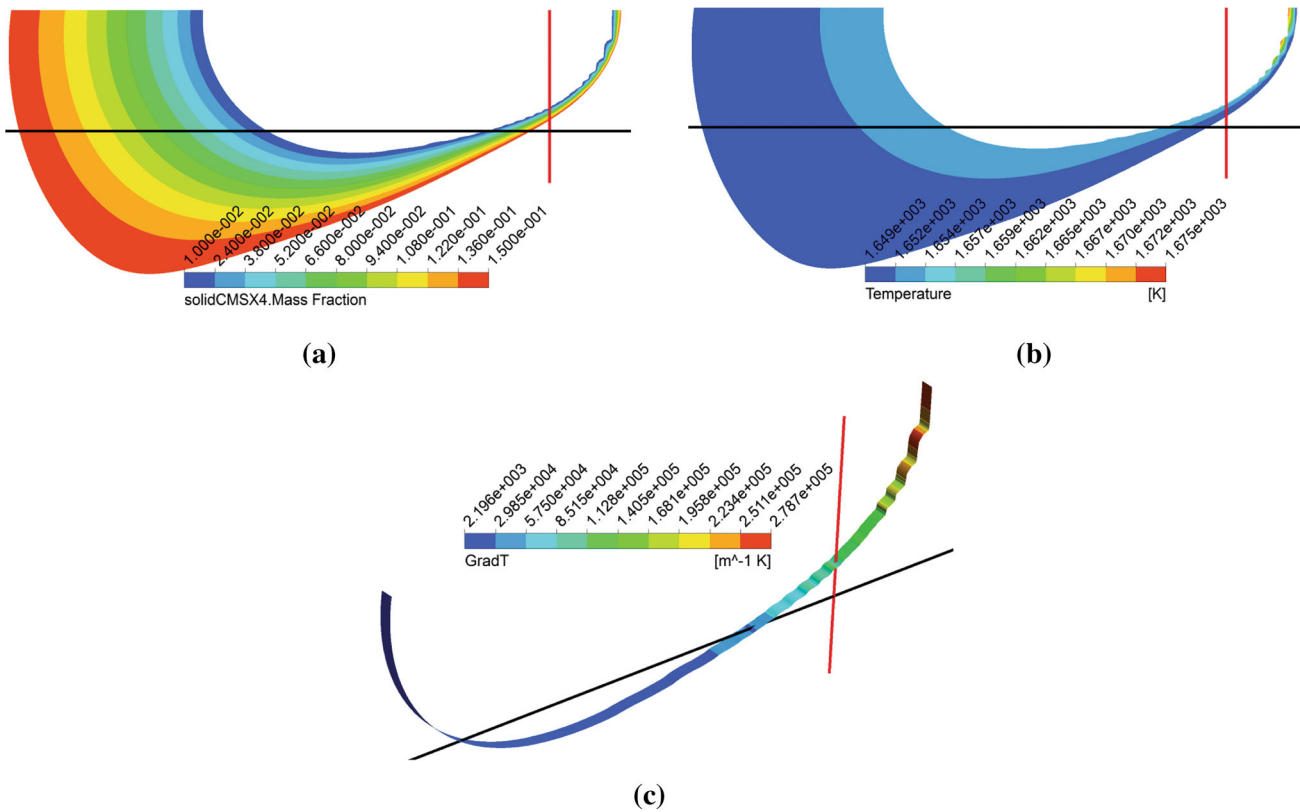


Fig. 9—(a) Identification of the mushy region, (b) contours of temperature in the mushy region due to the moving heat source in the CMSX-4 melt pool, and (c) representative contour of the temperature gradient in the CMSX-4 melt pool. The black lines indicate the original substrate position before laser processing, and the red lines indicate the instantaneous position of the laser. Laser movement direction is from the left to the right (Color figure online).

scan spacing resulted in a higher scan energy density and therefore expanded the melt pool and reduced the temperature gradient. This could expedite EQ grain formation, lowering the SX height as demonstrated in Figure 5(d). It was, therefore, critical to investigate and determine optimum parameter sets that would result in acceptable deposit characteristics.

Figure 6(a) provides a detailed view of two different microstructural transitions. The first transition is known as the oriented-to-misoriented transition or OMT. The single-crystal changes the growth direction from $\langle 001 \rangle$ to $\langle 100 \rangle$ primarily due to the change in the direction of the dominant temperature gradient as the substrate and the powder become increasingly hot toward the end of the scan.^[11] The second transition is known as the columnar-to-equiaxed/polycrystalline transition or CET. This occurs due to an increase in isotherm velocity near the surface and a decrease in the temperature gradient resulting in the formation of a constitutionally undercooled zone.^[10] Despite this loss of epitaxy due to CET and OMT, all SLE-processed samples showed SX deposit height of at least 500 μm . By optimizing the process parameters, the SX height could be further increased to 1000 μm in a single pass as shown in Figure 6(a).

Figure 6(b) provides a detailed view of the stray grain morphology. Due to the presence of local inhomogeneity in the temperature gradient and the solidification velocity, grains within the SX region can nucleate with

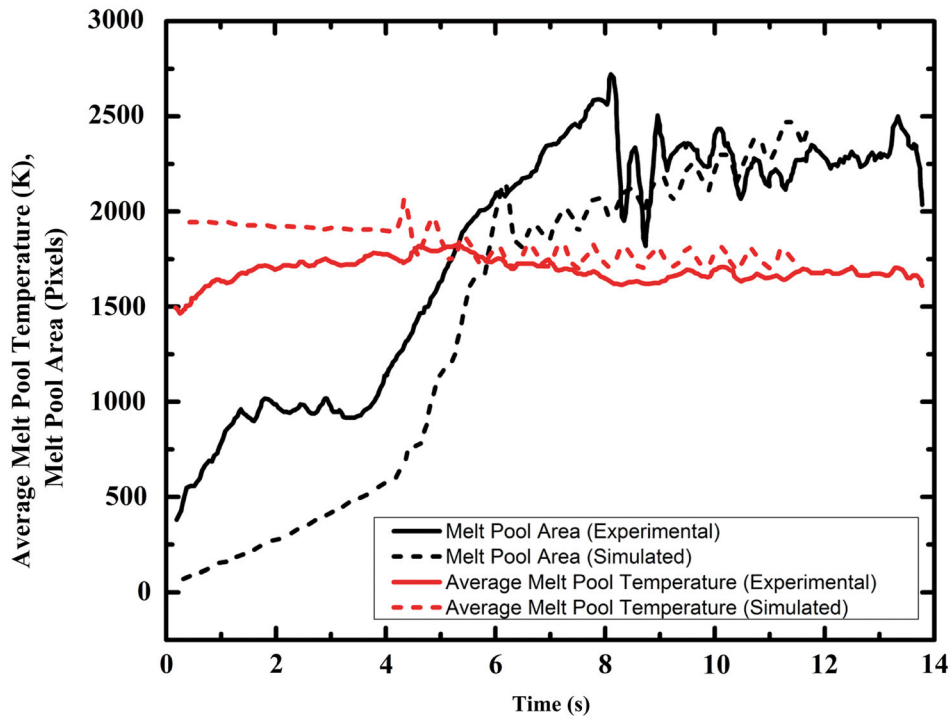
tilted boundaries. One reason for such stray grain formation is the breaking of secondary dendrite arms and convection of those broken pieces to a new location. The broken dendrite arms can act as sources of nucleation in the new site. Optimization of the SLE processing parameters can thus be useful to minimize the stray grain formation.

B. Analysis of the Microstructure Through Scanning Electron Microscopy (SEM)

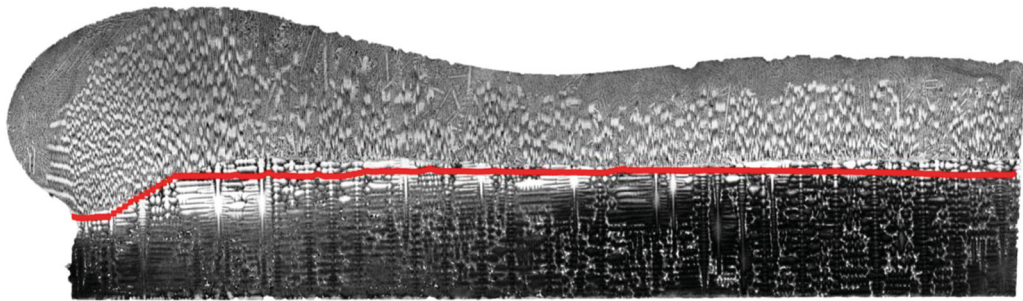
The SLE-deposited CMSX-4 samples were analyzed using SEM to characterize the microstructure. Figures 7(a) and (b) represent the SEM images of etched CMSX-4 in the substrate and deposit region, respectively. The primary γ' was of the order of 0.5 to 1 μm in the substrate region, while the secondary γ' was of the order of 50 nm. Microstructural refinement in the deposit region was observed as the primary γ' here was of order 100 nm as shown in Figure 7(b).

C. Effects of the SLE Processing Parameters on the Deposition Characteristics Using CFD

The effects of the SLE processing parameters on the melt pool characteristics were analyzed using the 2D CFD simulations. The moving energy source in SLE generated two vortices inside the melt pool as the laser



(a)



(b)

Fig. 10—(a) Comparisons of the simulated and experimentally obtained melt pool size and average temperature variation with time for the processing of CMSX-4 when observed from the top surface and (b) Comparisons of the simulated melt depth (red line) with the actual micrograph for CMSX-4 sample (Color figure online).

traveled over the substrate. Figures 8(a) and (b) show the velocity and temperature field generated inside the melt pool for CMSX-4, respectively. The melt pool was identified in the regions with liquid CMSX-4 mass fraction of 0.99 or more. This calculation was validated by the fact that inside the melt pool, the temperature was greater than 1654 K (1380.85 °C), the liquidus temperature of CMSX-4. The maximum velocity reached a value of 1.38 mm/s at the top of the melt pool while the bottom of the melt pool showed a velocity of 0.32 mm/s. The higher viscosity of CMSX-4 resulted in higher shear stress and forced the trailing edge vortex to follow the surface velocity pattern as shown in Figure 8(c). This showed up in the velocity vector plot inside the melt pool where the vortices were partially developed for CMSX-4 as opposed to IN100 which had lower liquid viscosity and thus showed fully developed vortices.^[29]

Figures 9(a) and (b) show the mushy zone and its temperature contour. The mushy zone showed temperature ranging from 1649 K to 1675 K (1375.85 °C to 1401.85 °C) in the representative scenario. Figure 9(c) shows the temperature gradient at the solid–liquid interface. The temperature gradient again reduced to 2.2×10^3 K/m at the trailing edge as compared to a value of 2.8×10^5 K/m at the leading edge.

Figure 10(a) shows the comparison of the experimentally obtained profile of the melt pool size and the average temperature with the simulated results for one particular CMSX-4 trial. The simulated melt pool size in the x-direction was multiplied with the sample width (70 pixels) to compute the melt pool size at the top surface. The IR camera also fixed the bounding box of the melt pool to 70 pixels. The melt pool extent in the x-direction obtained by simulation was lower at the beginning and of the order of 0.7 mm or 7 pixels, while the

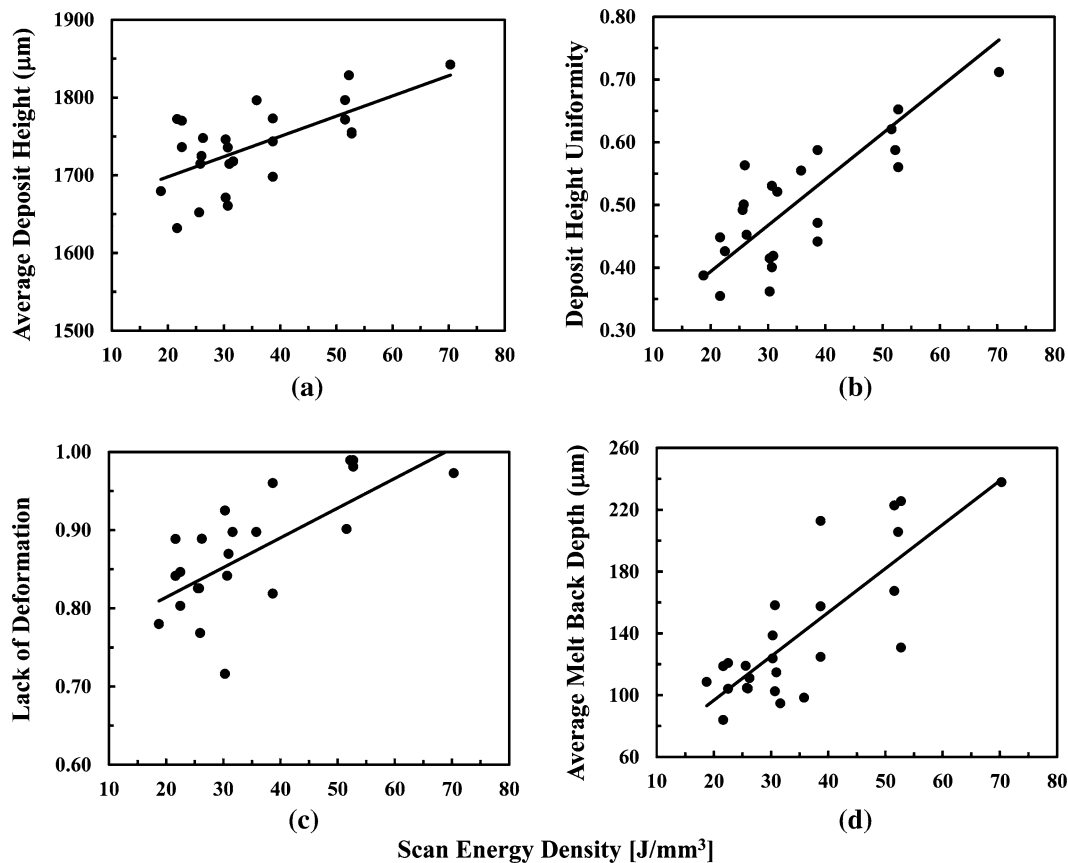


Fig. 11—Effect of scan energy density (E) on (a) average deposit height, (b) deposit height uniformity, (c) “lack of deformation,” and (d) average melt back depth for CMSX-4.

experimental value was close to 1.4 mm or 15 pixels. However, these two values gradually converged as the scan progressed. In the steady state, the value was close to 32 pixels or 3 mm in the x-direction. The simulation identified the melt pool if the liquid mass fraction is above 0.99. It might be possible that the molten powder and the mushy region ahead of the actual melt pool were detected by the IR camera. During the repeat scans, the anomaly was higher, since in reality the extension of the melt pool might not be gradual, and it could occur in discrete steps. The simulation predicted an average temperature in the range of 1900 K to 1800 K (1626.85 °C to 1526.85 °C), whereas the IR camera recorded an average temperature ranging from 1500 K to 1750 K (1226.85 °C to 1476.85 °C). Since the molten powders and mushy region were detected as melt pool by the IR camera, the average temperature value was reduced.

The melt depth profile was of particular importance for the present study, and hence, it was compared with the actual cross-sectional optical micrographs. Figure 10(b) illustrates the melt depth comparison between simulation and experimental results for CMSX-4, showing excellent agreement. The average melt depth for this particular experimental run was 98 μm . Multiple CFD simulations were performed to narrow down the SLE processing parameters to achieve the average melt depth of more than 75 μm but less than 175 μm . The desired average melt depth was of order 100 μm .

However, in the present study, a broader parameter range was explored to accurately characterize the effects of SLE processing parameters on the deposit. Higher values of E and Q increased the average melt depth, while lower values of E and Q resulted in interface fusion error between the substrate and the deposit region. Using the results from the 2D CFD model, the DoE runs were conducted with E in the 15 to 70 J/mm^3 range and Q in the 250 to 700 J/mm range.

D. Optimization of SLE Processing Parameters Using DoE-Based Approach

Figure 11(a) shows the effect of E on the average deposit height. Higher values of E caused the melt pool to expand drawing more powder inside the melt pool which increases the average deposit height. Figure 11(b) shows the effect of E on the deposit height uniformity. Higher values of E were associated with higher power and/or lower scan speed. Together, they caused a smoother flow of powder particles into the melt pool, thus removing surface instabilities. Figure 11(c) shows the effect of E on the “lack of deformation.” The higher the value of the “lack of deformation” parameter, the lower was the deformation amount. Higher values of E associated with lower scan speeds resulted in lower thermal lag, whereas lower values of E associated with higher scan speeds promoted thermal lag between the

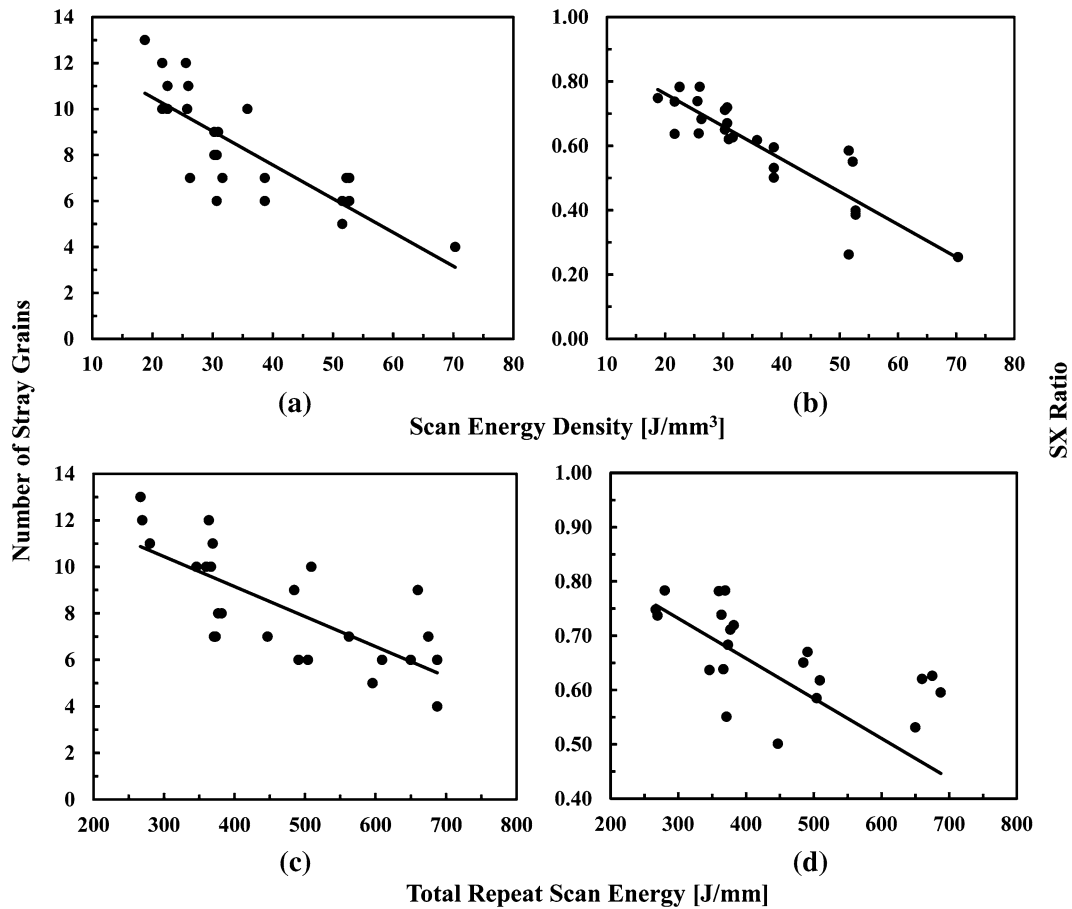


Fig. 12—Effect of scan energy density (E) on (a) number of stray grains, and (b) SX ratio for CMSX-4. Effect of total repeat scan energy (Q) on (c) number of stray grains and (d) SX ratio for CMSX-4.

melt pool and the bulk substrate. Thus, lower values of E caused more deformation and consequently lower value of the “lack of deformation” parameter in the substrate region. The average melt depth increased with an increase in E (Figure 11(d)) as more energy was being provided to the substrate in this case.

It was also observed that the number of stray grains decreased for higher values of E . The lower scan speeds and higher laser powers caused smoother flow of powder and lowered the Marangoni velocity at the top surface of the melt pool, thus decreasing the convection of broken dendrites. This reduced stray grain formation as shown in Figure 12(a). However, the SX ratio decreased significantly for higher values of E as shown in Figure 12(b). The higher laser powers and lower scan speeds expanded the melt pool, thus reducing the temperature gradient in the vertical direction. This caused nucleation of new grains due to constitutional undercooling resulting in lower SX ratios at higher values of E . Figure 12(c) shows the effect of Q on the number of stray grains. Higher values of Q decreased the number of stray grains as this ensured expansion of the melt pool causing a smoother flow of the powder toward the melt pool. The SX ratio also decreased as Q is increased as shown in Figure 12(d). An increase in Q increased the average substrate temperature and

decreased the vertical temperature gradient, thus lowering the SX height. SX ratios exceeding 0.5 and number of stray grains of less than 8 could thus be obtained simultaneously with E in the 35 to 50 J/mm^3 range and Q in the 400 to 500 J/mm range.

VI. CONCLUSIONS

The difficulties associated with the additive manufacturing of SX superalloys are well published.^[10,13,15] However, the present study conducted on the processing of SX CMSX-4 through SLE demonstrated the capability of the process in producing uniform deposits of CMSX-4 without any instances of cracking. The absence of cracking in the SLE process was due to a large amount of pre-heat and post-heat applied to each segment of the sample because of beam overlapping. The beam overlapping was ensured by scanning with extremely short scan spacing. The fabrication of dense, crack-free deposits of thickness exceeding 1000 μm , widths exceeding 6000 μm and lengths exceeding 35,000 μm with SX height of more than 500 μm using a tightly focused rastering fiber laser beam proved the capability of SLE as an additive manufacturing process for repair and manufacture of single-crystal hot section

components. The SX CMSX-4 deposit also showed refinements of the dendritic structure and reduction in the size of the primary γ' precipitates.

The pseudo-2D model built for the fiber laser allowed the flow field to be explored in shorter computation time as compared to a full 3D simulation. The model was previously validated for IN100.^[29] For CMSX-4, the model showed excellent agreement for the average melt pool temperature, melt pool area, and melt depth profile when compared to the experimental results. The shorter computation time was helpful in performing multiple CFD simulations. From the simulation results, the ranges of SLE processing parameters for the DoE experimental runs were chosen such that the simulated average melt depth was of order 75 to 175 μm .

DoE-based optimization was thereafter used to assess the effects of SLE processing parameters on the deposit quality. The deposit quality parameters were identified and calculated using an active contour-based image analysis technique. The image analysis code took the digital optical micrographs as input and calculated several analysis metrics such as the SX ratio, the average deposit height, the deposit height uniformity, the melt back depth, the number of stray grains, and the lack of deformation. Laser power, scan speed, and scan spacing were combined to define the scan energy density and the total repeat scan energy which served as critical parameters to characterize the SX deposit. Higher scan energy density expanded the melt pool drawing more powder inside the melt pool which increased the average deposit height and made the deposit uniform. Higher scan energy density also reduced the number of stray grains; however, it decreased the SX ratio. An increase in the SX ratio could be achieved by decreasing the values of E or increasing the scan speed which is a significant restriction in laser cladding systems. Such restriction arises from the fact that in the cladding or directed metal deposition processes, the speed of the energy source is limited by the speed of mechanical powder feed assembly. Powder bed-based systems hence can be proved beneficial in maintaining the epitaxy for SX superalloys.

Future efforts will include the fabrication of multi-layer deposits, and application of the CFD model to predict the melt depth profile for the same. Refinement in microstructure was observed in the present study. Such refinement theoretically can impart more strength to the deposit region. The effects of γ' precipitate size on the mechanical properties will be studied in future. Measurement of mechanical properties will include tensile, creep, and shear strength evaluation at elevated temperatures for the as-deposited and the heat-treated CMSX-4. Detail microstructural analysis will also be performed, and the effects of heat treatment on the microstructure will be reported in future studies.

ACKNOWLEDGMENTS

This work was sponsored by the Office of Naval Research through grants N00014-11-1-0670 and

N00014-14-1-0658. The authors would like to thank Mr. Parthasarathi Chakraborti, Packaging Research Center, Georgia Institute of Technology for his assistance with SEM.

DISCLOSURES

Dr. Suman Das is a co-founder of DDM Systems, a start-up company commercializing SLE technology. Dr. Das and Georgia Tech are entitled to royalties derived from DDM Systems' sale of products related to the research described in this paper. This study could affect their personal financial status. The terms of this arrangement have been reviewed and approved by Georgia Tech in accordance with its conflict of interest policies.

REFERENCES

1. R.C. Reed: *The Superalloys: Fundamentals and Applications*, Cambridge University Press, New York, 2006.
2. J.K. Tien: *Superalloys, Supercomposites and Superceramics*. (Elsevier, 2012).
3. D.J. Frasier, J.R. Whetstone, K. Harris, G.L. Erickson, R.E. Schwer, *High Temperature Materials for Power Engineering*, 1990, pp. 1281–1300.
4. A.F. Giamei, D.D. Pearson and D.L. Anton, In *MRS Proceedings*, (Cambridge University Press, Cambridge, 1984), pp 293–308.
5. J. Rüsing, N. Wanderka, U. Czubyko, V. Naundorf, D. Mukherji, and J. Rösler: *Scripta Mater.*, 2002, vol. 46, pp. 235–40.
6. A. Mottura, N. Warnken, M.K. Miller, M.W. Finnis, and R.C. Reed: *Acta Mater.*, 2010, vol. 58, pp. 931–42.
7. A. Sengupta, S.K. Putatunda, L. Bartosiewicz, J. Hangan, P.J. Nailos, M. Peputapeck, and F.E. Albers: *J. Mater. Eng. Perform.*, 1994, vol. 3, pp. 73–81.
8. M.J. Donachie and S.J. Donachie: *Superalloys: A Technical Guide*, ASM international, Materials Park, 2002.
9. M. Lamm and R.F. Singer: *Metall. Mater. Trans. A*, 2007, vol. 38A, pp. 1177–83.
10. M. Gäumann, C. Bezencon, P. Canalis, and W. Kurz: *Acta Mater.*, 2001, vol. 49, pp. 1051–62.
11. S. Mokadem, C. Bezençon, A. Hauert, A. Jacot, and W. Kurz: *Metall. Mater. Trans. A*, 2007, vol. 38A, pp. 1500–10.
12. A. Gregori and D. Bertaso: *Weld. World*, 2003, vol. 51, pp. 34–47.
13. S.S. Babu, S.A. David, J.W. Park, and J.M. Vitek: *Sci. Technol. Weld. Join.*, 2004, vol. 9, pp. 1–12.
14. M.B. Henderson, D. Arrell, R. Larsson, M. Heobel, and G. Marchant: *Sci. Technol. Weld. Join.*, 2004, vol. 9, pp. 13–21.
15. M. Gäumann, S. Henry, F. Cleton, J.-D. Wagniere, and W. Kurz: *Mater. Sci. Eng. A*, 1999, vol. 271, pp. 232–41.
16. C. Bezencon, A. Schnell, and W. Kurz: *Scripta Mater.*, 2003, vol. 49, pp. 705–09.
17. R. Vilar, E.C. Santos, P.N. Ferreira, N. Franco, and R.C. Da Silva: *Acta Mater.*, 2009, vol. 57, pp. 5292–5302.
18. E.C. Santos, K. Kida, P. Carroll, and R. Vilar: *Adv. Mater. Res.*, 2011, vols. 154–155, pp. 1405–14.
19. L.E. Murr: *Addit. Manuf.*, 2015, vol. 5, pp. 40–53.
20. M. Ramsperger, L. Mújica Roncery, I. Lopez-Galilea, R.F. Singer, W. Theisen, and C. Körner: *Adv. Eng. Mater.*, 2015, vol. 17, pp. 1486–93.
21. T.D. Anderson, J.N. DuPont, and T. DebRoy: *Acta Mater.*, 2010, vol. 58, pp. 1441–54.
22. T.H.C. Childs, C. Hauser, and M. Badrossamay: *CIRP Ann. Manuf. Technol.*, 2004, vol. 53, pp. 191–94.
23. M. Picasso and A.F.A. Hoadley: *Int. J. Numer. Methods Heat Fluid Flow*, 1994, vol. 4, pp. 61–83.
24. D.V. Bedenko and O.B. Kovalev: *Thermophys. Aeromech.*, 2013, vol. 20, pp. 251–61.

25. Z. Liu and H. Qi: *Metall. Mater. Trans. A*, 2014, vol. 45A, pp. 1903–15.
26. J. Mazumder: *Opt. Eng.*, 1991, vol. 30, pp. 1208–19.
27. W. Liu and J.N. DuPont: *Acta Mater.*, 2004, vol. 52, pp. 4833–47.
28. R. Acharya, R. Bansal, J.J. Gambone, and S. Das: *Metall. Mater. Trans. B*, 2014, vol. 45B, pp. 2247–61.
29. R. Acharya and S. Das: *Metall. Mater. Trans. A*, 2015, vol. 46, pp. 3864–75.
30. S. Das: *Adv. Eng. Mater.*, 2003, vol. 5, pp. 701–11.
31. R. Acharya, R. Bansal, J.J. Gambone, and S. Das: *Metall. Mater. Trans. B*, 2014, vol. 45B, pp. 2279–90.
32. R. Acharya, R. Bansal, J.J. Gambone, M.A. Kaplan, G.E. Fuchs, N.G. Rudawski, and S. Das: *Adv. Eng. Mater.*, 2015, vol. 17, pp. 942–50.
33. J.J. Gambone, (MS Thesis, Georgia Institute of Technology: 2012).
34. R. Acharya, (Ph.D. Thesis, Georgia Institute of Technology: 2014).
35. I. Hamill, (Technical Report, CFX Ltd., Oxfordshire, 2003).
36. W.L. McCabe, J.C. Smith, and P. Harriott: *Unit Operations of Chemical Engineering*, McGraw-Hill, New York, 1993.
37. L.X. Yang, X.F. Peng, and B.X. Wang: *Int. J. Heat Mass Transfer*, 2001, vol. 44, pp. 4465–73.
38. T. Matsushita, H.-J. Fecht, R.K. Wunderlich, I. Egry, and S. Seetharaman: *J. Chem. Eng. Data*, 2009, vol. 54, pp. 2584–92.
39. Y.S. Lee, M. Nordin, S.S. Babu, and D.F. Farson: *Weld. J.*, 2014, vol. 93, pp. 292–300.